**An Assessment of the Impact of ATMS and CrIS Data Assimilation on Precipitation Prediction over the Tibetan Plateau**

Tong Xue[1, 2, 4, 5], Jianjun Xu[2, 3], Zhaoyong Guan[1], Han-Ching Chen[5, 6], Long S. Chiu[5], Min Shao[7]

[1]Key Laboratory of China Education Ministry for Meteorological Disasters, Nanjing University of Information Science and Technology, Nanjing, China

[2]Guangdong Ocean University, Zhanjiang, China

[3]State Key Laboratory of Severe Weather, Chinese Academy of Meteorological Sciences, China

[4]China Meteorological Administration Training Centre, Beijing, China

[5]AOES, College of Science, George Mason University, Fairfax, Virginia, USA

[6]Department of Atmospheric Sciences, National Taiwan University, Taipei, Taiwan

[7]GENRI, College of Science, George Mason University, Fairfax, Virginia, USA

*Correspondence to*: Jianjun Xu ,Guangdong Ocean University, Zhanjiang, China (gdouxujj@qq.com) and Han-Ching Chen, National Taiwan University, Taipei, Taiwan , (s910810909@gmail.com)

24 **Abstract**

25     Using the National Oceanic and Atmospheric Administration's Gridpoint Statistical

26 Interpolation data assimilation system and the National Center for Atmospheric Research's

27 Advanced Research Weather Research and Forecasting (WRF-ARW) regional model, the impact

28 of assimilating advanced technology microwave sounder (ATMS) and cross-track infrared

29 sounder (CrIS) satellite data on precipitation prediction over the Tibetan Plateau in July 2015

30 was evaluated. Four experiments were designed: a control experiment and three data assimilation

31 experiments with different data sets injected: conventional data only, a combination of

32 conventional and ATMS satellite data, and a combination of conventional and CrIS satellite data.

33 The results showed that the monthly mean of precipitation is shifted northward in the simulations

34 and shows an orographic bias described as an overestimation in the upwind of the mountains and

35 an underestimation in the south of the rainbelt. The rain shadow mainly influenced prediction of

36 the quantity of precipitation, although the main rainfall pattern was well simulated. For the first

37 24-hour and last 24-hour accumulated daily precipitation, the model generally overestimated the

38 amount of precipitation, but it was underestimated in the heavy rainfall periods of 3-5, 13-16,

39 and 22-25 July. The observed water vapor conveyance from the southeastern Tibetan Plateau was

40 larger than in the model simulations, which induced inaccuracies in the forecast of heavy rain on

41 3–5 July. The data assimilation experiments, particularly the ATMS assimilation, were closer to

42 the observations for the heavy rainfall process than the control. Overall, based on the

43 experiments in July 2015, the satellite data assimilation improved to some extent the prediction

44    of precipitation pattern over the Tibetan Plateau although the simulation of rainbelt without data

45    assimilation shows the regional shifting.

46    **Key words:** Radiance data assimilation, GSI, Tibetan Plateau, Weather forecast accuracy

**1. Introduction**

The Tibetan Plateau (TP) is the highest and largest plateau in the world. It is located in the central Eurasian continent and stands in the middle troposphere, covering an area of approximately 2.5 million km$^2$. The TP has a variety of topographical features of a large terrain gradient and its steep mountains are aligned with an east-to-west arrangement. The dramatic modification caused by the rugged terrain influences the local atmospheric circulation and causes strong local convection to arise, easily inducing severe weather such as heavy rainfall, windstorms, hailstorms, and so on (Massacand et al., 1998; Gao et al., 2015). Precipitation is one of the key variables for understanding the hydrological cycle on the TP and has profound effects on the regional and global circulation that affect millions of people in the adjacent areas (Ye and Gao, 1979; Chen et al., 1985; Chambon et al., 2014). Therefore, making accurate and long-lead weather forecasts at high temporal and spatial resolution for the TP not only has scientific significance but also addresses the urgent need for disaster prevention. However, due to the variable weather conditions and complex terrain orography, the TP remains a sparsely populated region with few conventional observation data sources, and the limited available meteorological data leads to great uncertainties in the regional weather forecasts. The continuous development of numerical weather prediction (NWP) models, such as the National Center for Atmospheric Research (NCAR)'s Advanced Research Weather and Research Forecasting (WRF-ARW) model, offer opportunities to improve regional weather forecasts in data-sparse regions. NWP models can be initialized with and laterally assimilate observation data, which is beneficial for better

68  describing atmospheric conditions, thus keeping model results close to observations (Maussion et

69  al., 2011).

70    Satellite radiance data are one of the most important observation data sources and can be

71  directly assimilated into data assimilation models. Compared with conventional observation data,

72  geostationary satellite data have continuous spatial and temporal coverage and polar orbiting

73  satellites circle the earth twice a day to provide global observations of multiple meteorological

74  variables, such as temperature, pressure, moisture, and so on. Moreover, many studies have

75  suggested that the assimilation of satellite radiance data can substantially improve weather

76  forecasts (Eyre, 1992; Derber and Wu, 1998; Xu et al., 2009). For longer-range prediction,

77  satellite data are even more crucial than conventional observations (Zapotocny et al., 2008). Past

78  studies have also indicated that the effect of assimilation of both observations and satellite

79  products was better than only satellite data assimilation (Liu et al., 2013).However, the

80  performance of satellite radiance assimilation in limited-area modeling systems using variational

81  DA method is still controversial (Zou et al., 2013; Newman et al., 2015).Schwartz et al. (2012)

82  was the first to assimilate microwave radiances with the region lacking observation stations

83  using ensemble Kalman filter (ENKF) and the results showed that assimilating microwave

84  radiances overall make better forecasts of Typhoon Morakot (2009). The negative influence has

85  also appeared and it is mainly contributed to various of factors such as the influence of lateral

86  boundary conditions within the regional domain (Warner et al., 1997) and non-uniform satellite

87  coverage (Kazumori et al., 2014).

88    The advanced technology microwave sounder (ATMS) and cross-track infrared sounder

89    (CrIS) are two instruments with high resolution onboard the Suomi National Polar-orbiting

90    Partnership spacecraft a polar-orbiting satellite launched in 2011 with the aim to provide real-

91    time sensor data for critical weather and climate measurements. The ATMS, a cross-track

92    microwave scanner with 22 channels, combines most of the channels of the preceding advanced

93    microwave sounding unit (AMSU-A) and microwave humidity sounder (MHS) to provide

94    sounding profiles of atmospheric moisture and temperature. The CrIS is a Fourier transform

95    spectrometer with 1305 spectral channels inherited from the high-resolution infrared radiation

96    sounder (HIRS) to produce temperature, pressure, and moisture profiles. A previous study

97    assimilated ATMS data in the European Centre for Medium-Range Weather Forecasts system

98    and the results showed that the instrument had better performance than AMSU-A and MHS in

99    the longer range over the Northern Hemisphere (Bormann et al., 2013). Nevertheless, satellite

100   data assimilation into NWP models over the TP presents special challenges, because the limited

101   model capability for assimilating radiance data over complex terrain with heterogeneous

102   characteristics is still not clearly recognized. Furthermore, whether the new generation of

103   satellite observations, such as ATMS and CrIS, can compensate for the shortage of data over the

104   TP and effectively enhance the accuracy of forecasts remains unknown.

105       In this paper, we make an assessment of the impact of assimilating ATMS and CrIS radiance

106   data for East Asia on precipitation prediction over the TP and compare the effects of different

107   satellite data sets injected.

**2. Data and Models**

*2.1 Data*

*2.1.1 Data used for the assimilation*

The conventional data which is from the Global Data Assimilation System (GDAS)-prepared BUFR files (gdas1.tCCz.prepbufr.nr) is composed of a global set of surface and upper air reports operationally collected by the National Centers for Environmental Prediction (NCEP). It includes radiosondes, surface ship and buoy observations, surface observations over land, pilot balloon (pibal) winds and aircraft reports from the Global Telecommunications System (GTS), profiler and US radar derived winds, Special Sensor Microwave Imager (SSM/I) oceanic winds and atmospheric total column water (TCW) retrievals, and satellite wind data from the National Environmental Satellite Data and Information Service (NESDIS). The reports can include pressure, geopotential height, temperature, dew point temperature, wind direction and speed. (National Centers for Environmental Prediction/National Weather Service/NOAA/U.S. Department of Commerce. 2008, updated daily. *NCEP ADP Global Upper Air and Surface Weather Observations (PREPBUFR format), May 1997 - Continuing.* )

ATMS and CrIS satellite radiance data are also from the GDAS which is in the BUFR format. All of this can be downloaded from https://www.ncdc.noaa.gov/data-access/model-data/model-datasets/global-data-assimilation-system-gdas.

*2.1.2 Data used for the evaluation/verification*

128    Observational precipitation data from the National Meteorological Information Center (NMIC)

129    of the China Meteorological Administration (CMA) was used as the truth data for comparison

130    with the model results. The $0.1° \times 0.1°$ high-resolution gridded hourly China Merged

131    Precipitation Analysis (CMPA) data gauge, which combines the CMA's rain gauge hourly data

132    provided by more than 30,000 automatic weather stations with the National Oceanic and

133    Atmospheric Administration (NOAA) Climate Prediction Center's Morphing (CMORPH)

134    precipitation product (Xie & Xiong, 2011; Pan et al., 2012; Shen et al., 2014), was used for

135    verification to evaluate the model simulation results. Considering the topographically complex

136    terrain characterizing the TP, satellite precipitation data with very high spatial resolution is

137    especially needed. CMORPH product makes use of the precipitation estimates technique that

138    have been derived from low orbiter satellite microwave observations and geostationary satellite

139    IR data with spatial propagation features. Several studies (Gao et al., 2013; Guo et al., 2014;

140    Tong et al., 2014; Zhang et al., 2015) have compared the CMORPH data with satellite

141    precipitation data sets in the TP area with the conclusion that CMORPH data is one of the most

142    suitable product to use in studying precipitation over the TP. During the period from May to

143    October 2004-2009, Tropical Rainfall Measuring Mission (TRMM) Multisatellite Precipitation

144    Analysis real-time research 3B42 version 6 (TMPA) and CMORPH show better performance in

145    higher correlation and lower RMSE than the Precipitation Estimation from Remotely Sensed

146    Information using Artificial Neural Network (PERSIANN) and TMPA's real time version

147    (TMPART) over the TP(Gao et al., 2013). Of the several merged satellite precipitation products

148    (i.e.TMPA, PERSIANN, and the Global Satellite Mapping of Precipitation (GSMaP)), the

149    CMORPH product with the highest resolution (8 km) can capture the afternoon-to-evening

150    precipitation pattern (Guo et al.,2014). Tong (2014) has also compared the performance of four

151    widely-used high resolution satellite precipitation estimates against gauge observations (the

152    CMA data) over the TP during January 2006-December 2012. It's worth noticing that TMPA and

153    CMORPH data had better performance in depicting precipitation timing and amount than the

154    TMPART and PERSIANN at both the plateau and basin scale. Zhang (2015) has also made a

155    conclusion that the high resolution CMORPH data can depict finer regional details, such as a less

156    coherent phase pattern over the TP and better capture the features of the diurnal cycle of summer

157    precipitation compared with TRMM 3B42.

158    NCEP Final Analysis (FNL) data was used through dynamic downscaling as observed

159    moisture to illustrate the transportation of water vapor in East Asia.

160

161    *2.1.3  Radiance data quality control*

162    As the quality of the observational data is easily affected by the observation instruments,

163    station positions, or human factors, carrying out quality control before data application is

164    necessary (Hubbard and You, 2005). Before data assimilation, a multiple-step quality control

165    procedure was applied to the satellite radiance data in the GSI system and preprocessed by

166    NOAA's Satellite and Information Service (NESDIS). Besides data thinning, it can be

167    summarized to several quality control (QC) categories in GSI to either toss the questionable

168    observations or inflate the low confidence observations. The detailed quality control can be

169    found in the section 8.3 radiance observation quality control in the Gridpoint Statistical

170    Interpolation (GSI) Advanced User's Guide version 3.5 by Developmental Testbed Center (DTC)

171    (2016).  The observational number of ATMS data ranging from 53042 to 68618 in contrast to the

172    number of CrIS data ranging from 2694048 to 3454542 are read in DA system. After the data had

173    passed rigorous quality assessment and quality control processes, the results showed that about

174    23.2%-26.4%, and 1.3% and 1.6% of "good" observations related to ATMS and CrIS read data

175    separately were retained after quality control (Fig. 2). This difference can be explained that CrIS

176    has 1305 channel satellite radiance data, but the number of assimilated channels are significantly

177    reduced (Table 1),  the selection of redundant channel leads to some part of observation radiance

178    data comes from the similar altitude and contains large amount of repeated information.

179    Therefore, larger percentage of CrIS satellite radiance data than ATMS is tossed through QC

180    steps. Figure 1(b) shows the distribution of the conventional data at 06:00 UTC on 1 July 2015,

181    where observational data are rare in the TP. Figure 1c and 1d displays the distribution of satellite

182    data after quality control, where there is almost complete spatial coverage in East Asia including

183    the TP.

184

185    *2.2 Models*

186    *2.2.1 WRF-ARW regional model*

187        NCAR's WRF-ARW regional model associated with the Gridpoint Statistical Interpolation

188     (GSI) data assimilation system was used in this study. WRF-ARW is a fully compressible

189     nonhydrostatic, primitive-equation, mesoscale meteorological model. As shown in Figure 1a, the

190     model domains are two-way nested with 12 km (580 × 422) and 4 km (817 × 574) horizontal

191     spacing. There are 51 vertical levels with a model top of 10 hPa. Figure 1 shows that D01 is set

192     to cover most of East Asia and the subdomain (D02) inside corresponds to the Tibetan Plateau,

193     which has a mountain–valley structure.

194         The physical parameterizations chosen for the forecast model in this study followed previous

195     studies of the area (He et al., 2012; Xu et al., 2012; Zhu et al., 2014). These included the WRF-

196     ARW Single-Moment 6-class (WSM-6) microphysics scheme, the Kain-Fritsh (KF) cumulus

197     parameterization, the Rapid Radiative Transfer Model (RRTMG) longwave and shortwave

198     radiation, the Yonsei University scheme (YSU) and the Noah Land Surface Model for the

199     planetary boundary layer scheme.

200         The National Centers for Environmental Prediction (NCEP) global forecast system (GFS)

201     forecast data, which has a horizontal resolution of 0.5° × 0.5° with a 6-hour interval, were used

202     as the boundary and initial conditions for the control (CTRL) experiment, while the background

203     fields of data assimilation experiments (DA) take advantages of the forecast product at 06:00

204     UTC made by CTRL. The GFS data are publicly available from https://www.ncdc.noaa.gov/data-

205     access/model-data/model-datasets/global-forcast-system-gfs.

206

207     *2.2.2 The GSI 3D-Var system and Community Radiative Transfer Model*

208    In this study, we chose to use the GSI 3D-Var system, which is a data assimilation system

209    that was initially developed as the next-generation analysis system based on the operational

210    Spectral Statistical Interpolation (SSI) at NCEP (Derber and Wu, 1998).

211    Instead of the spectral definition of backgrounds errors in the SSI, GSI is constructed in

212    physical space which the background errors can be represented by a non-homogeneous and

213    anistropic gridpoint and used for both global and regional forecasts. GSI utilizes recursive filters

214    and is designed to be a flexible system that is efficient on available parallel computing platforms

215    (Wu et al., 2002; Purser et al., 2003a, b). The GSI 3D-Var system provides an optimal analysis

216    through two outer iterative minimization of a prescribed function as follows:

217    $J = \frac{1}{2}(x_a - x_b)^T B^{-1}(x_a - x_b) + \frac{1}{2}(H(x) - O_o)^T O^{-1}(H(x) - O_o)$    (1)

218    Where $x_a$ is the analysis state can be calculated by minimizing the penalty function J, $x_b$ is

219    the first guess that comes from GFS product in this article representing background model state,

220    $O_o$ are the observations including conventional observation, satellite radiance data, radar data,

221    etc. $H(x)$ is the transformation operator from the analysis variable to the form of the $O_o$ error. By

222    means of the two sources of priori data: the first guess $x_b$ and the observations $O_o$, the solution

223    for the penalty function which indicates the posteriori maximum likelihood estimate of the true

224    atmospheric state can be found. While B and O are the error estimates of $x_b$ (covariance matrix

225    of the background error) and $O_o$ (covariance matrix of the observation error) respectively which

226    are used to weight the analysis fit to individual observations (Wu et al., 2002).

227    The development of fast radiative transfer models has allowed for the direct assimilation of

228     satellite infrared and microwave radiances in NWP systems (Saunders et al., 1999; Gauthier et

229     al., 2007; Zou et al., 2011). The Community Radiative Transfer Model (CRTM) developed by the

230     United States Joint Center for Satellite Data Assimilation (JCSDA) has been incorporated into

231     the NCEP GSI system to rapidly calculate satellite radiances (Han et al., 2006; Weng, 2009).

232     After ATMS and CrIS data are read into the GSI, simulated brightness temperature are calculated

233     via CRTM 2.1.3 in this study. It is worth noticing that the CrIS scans a 2200km swath width (+/-

234     50 degrees), with 30 Earth-scene views. Each field consists of 9 fields of view, arrayed as 3x3

235     array of 14km diameter spots (nadir spatial resolution). (https://jointmission.gsfc.

236     nasa.gov/cris.html). The ATMS scans a 2300km swath width with 96 Earth-scene views. The 1-2

237     channel of the spatial resolution of ATMS at nadir is 75km; 3-6 channel is 32km; 17-22 channel

238     is 16km (Dong et al., 2014).

239

240     **3. Method and experimental design**

241     *3.1 Method*

242         A basic two-by two contingency table (Table 2) was generated to calculate the Bias Score

243     (BIAS), Fraction skill Score (FSS), Equitable Threat Score (ETS), Probability of False Detection

244     (POFD), Probability of Detection (POD), and False Alarm ratio (FAR).

245         The BIAS (Range: $0\sim\infty$, Perfect score: 1), which measures the ratio of the frequency of

246     forecast events to the frequency of observed events, is defined as:

247     $$\text{BIAS} = \frac{\text{Hits+False alarms}}{\text{Hits+Misses}} \qquad (2)$$

248     The FSS (Range: 0~1, Perfect score: 1) introduced by Roberts and Lean (2008) is a

249     neighborhood verification method. The FSS is defined as:

250
$$\text{FSS} = 1 - \frac{FBS}{FBS_{ref}}$$
(3)

251     Fractions Brier Score (FBS) is presented as

252
$$\text{FBS} = \frac{1}{N}\sum_{i=1}^{N}[F_o - F_f]^2$$
(4)

253     Where $N$ is the number of all grid points in the domain. $F_o$ and $F_f$ are the observation and

254     forecast fractions of the sliding window at each grid point. The sliding window in this study is

255     100km (25 grid points). The reference Fractions Brier Score ($FBS_{ref}$) represent a largest possible

256     FBS and is given as:

257
$$FBS_{ref} = \frac{1}{N}\left[\sum_{i=1}^{N}F_o{}^2 + \sum_{i=1}^{N}F_f{}^2\right]$$
(5)

258     The ETS (Range: -1/3~1, Perfect score: 1) computes the fraction of observed events that were

259     correctly predicted:

260
$$\text{ETS} = \frac{\text{Hits} - R}{\text{Hits} + \text{False alarms} + \text{Misses} - R}$$
(6)

261     where R is the random forecast coefficient, given by:

262
$$R = \frac{(\text{Hits} + \text{False alarms})(\text{Hits} + \text{Misses})}{(\text{Hits} + \text{False alarms} + \text{Misses} + \text{Correct rejections})}$$
(7)

263     The POFD (Range: 0~1, Perfect score: 0) measures discrimination:

264
$$\text{POFD} = \frac{\text{False alarms}}{\text{False alarms} + \text{Correct rejections}}$$
(8)

265     Similar to the POFD, the POD (Range: 0~1, Perfect score: 1) shows the hits out of total observed

266     events:

267
$$\text{POD} = \frac{\text{Hits}}{\text{Hits} + \text{Misses}}$$
(9)

268    The FAR (Range: 0~1, Perfect score: 0) indicates the fraction of the predicted events that did not

269    occur:

270    $$FAR = \frac{False\ alarms}{Hits + False\ alarms}$$    (10)

271    To compare the model simulation data with the observation data, the 4-km model grid was

272    interpolated to observation data with $0.1° \times 0.1°$ degree grid based on linear interpolation method.

273

274    *3.2 Experimental design*

275        Four one-month-long experiments were conducted (Fig. 3). The CTRL experiment was

276    carried out first with an initial time of 00:00 UTC and made 54 h forecasts. The data assimilation

277    was applied on the D01 region of the output from CTRL at 06:00 UTC. The DA experiments

278    made use of the assimilated D01 and the D02 from the CTRL at 06:00 UTC as the initial

279    condition and made a 48 h forecast for each day. Three DA experiments were performed with a

280    time window of 3 hours: (1) a conventional run (CONV) assimilating the conventional

281    observation data only; (2) an ATMS radiance run (ATMS) adding the ATMS satellite radiance

282    data to the CONV; and (3) a CrIS radiance run (CRIS) adding the CrIS satellite radiance data to

283    the CONV.

284        The accumulated precipitation integrated from 06 to 30 h and 30 to 54 h are defined as the

285    first twenty-four-hour accumulated (F24H) precipitation and last twenty-four-hour accumulated

286    (L24H) precipitation, respectively.

287

 **4. Results**

 *4.1 Impact of DA on the spatial fields of precipitation forecast*

290     Figure 4 shows the spatial pattern of the monthly mean of 24-hour accumulated precipitation

291 in July 2015. Monthly mean precipitation exhibits a decreasing south-to-north gradient. The

292 predicted precipitation in the central and northern parts of the TP, Qaidam Basin (90°-99°E, 35°-

293 39°N), Tarim Basin (75°-90°E, 37°-42°N), and Junggar Basin (80°-90°E, 45°-48°N) was too

294 small to be measured (Fig. 4a, c). It was found that monthly averaged F24H precipitation ranged

295 from 6.0 to 30.4 mm/day, while the monthly averaged L24H precipitation ranged from 6.0 to

296 29.5 mm/day. The rain shadow along the Himalayas (73°-95°E, 27°-35°N) was found in the

297 spatial distribution of precipitation. Due to the Figure 4 (a) standing for the F24H, the first day

298 calculated in Figure 4 (a) was during the period of 06:00 UTC 1$^{st}$ July to 06:00 UTC 2$^{nd}$ July and

299 finally ended in the period of 06:00 UTC 29$^{th}$ July to 06:00 UTC 30$^{th}$ July. Therefore the

300 different values in Figure 4 (a) and (c) can be explained that the Figure 4 (c) shows the L24H

301 observed monthly mean accumulated precipitation of which the computing process are different

302 in in two days with Figure 4 (a).  The CTRL (Fig. 4b, d) mostly simulated the monthly mean

303 rainbelt distributed along the southern and southwestern margin of the plateau, between the

304 Himalayas in the west and the Hengduan Mountains (95°-103°E, 24°-32°N) in the east. The

305 difference between the model simulations and observations (Fig. 5) indicated that the CTRL

306 simulation tends to overestimate precipitation, especially in the southern and southwestern

307 margin along the rainbelt where the altitude changes from 500 to 3000 m. The results suggested

308    that the WRF-ARW model has limitations in simulating the precipitation in mountainous areas,

309    which is similar to the conclusion of previous studies (He et al., 2012; Xu et al., 2012).

310    Furthermore, we found that the precipitation is overestimated (colored red) in the upwind of the

311    mountains along the southwestern margin. In contrast, the precipitation is underestimated in the

312    south of the rainbelt, leading to a north–south dipole structure. This pattern results in a northward

313    migration of the rainbelt in the simulations. The three DA experiments indicated that the

314    assimilation of satellite radiance data can not calibrate the rain shadow effect and all experiments

315    showed consistently gross overestimation patterns, varying from 8 to 10 mm about the monthly

316    mean daily precipitation. The overall bias statistic in D02 is 0.97 mm (0.86 mm), 0.52 mm (0.70

317    mm), 1.08 mm (0.97 mm), and 0.98 mm (0.76 mm) CTRL, CONV, ATMS and CRIS

318    respectively. The values in brackets are referred to L24h. This may be attributed to the physical

319    package of WRF-ARW having an inadequate description of snow cover over the plateau surface

320    making the error of margin more prominent (Marteau et al. 2015).

321        Figure 6 shows the spatial patterns according to the contingency table (Table 2) and the

322    scatter plots, in which monthly mean 24 h rainfall over the 6 mm/day threshold is defined as an

323    "event". Rainfall events occur over most of the TP area, including the northern Gangetic Plain

324    (80°-90°E, 24°-28°N) where the elevation is lower than 3000 m, and can be well predicted with

325    ~8–10% hits (A) and ~76–79% correct rejections (D) in the majority of the region. The false

326    alarms (B) were spread mainly in the east of the TP, where the Bayan Har (95°E, 35°N) and

327    Hengduan mountains are located, accounting for ~7–10%, while the misses (C) were distributed

328    in the western plain exterior of the TP and accounted for ~5–6%. It's also evident to see the

329    dipole pattern in the distribution of the hits and misses similar to the Figure 5. Among the four

330    linear regression lines (bold grey lines), ATMS looks a little better than the other three

331    experiments but has more extreme-precipitation event forecasts than the others, followed by the

332    CTRL and CRIS, while CONV has the lowest simulation precision. The ~84-89% high

333    percentage of hits and correct rejections events indicates that rainfall events are well predicted.

334    Furthermore, as the false alarms were primarily located in the east of the TP in contrast to the

335    misses in the west, this special pattern can help improving WRF-ARW forecasts in the future

336    which means that WRF-ARW model has promising potential in TP area.

337        Figure 7 shows the monthly and domain average validation statistics in the TP. The

338    differences between the four experiments for the F24H forecasts are larger than for the L24H

339    forecasts. The ETS, FSS, and POD values all decline as the threshold increases; a higher value

340    for these three skill scores indicates a better performance of the experiments. ATMS showed the

341    highest FSS (Fig. 7b), ETS (Fig. 7c) and POD (Fig. 7d). CONV performed similar to the CTRL

342    in ETS and FSS, and CRIS performed the worst. However, according to the BIAS, CONV is

343    mostly approximately 1, which indicates the best overall relative frequencies compared with the

344    other experiments. Through the 1–5 mm threshold, CRIS performs the largest overforecast

345    (BIAS > 1), but it evolves to have a better performance than ATMS and CTRL through the 5–10

346    mm threshold. FAR and POFD results indicate that CONV performs best (0 is perfect), followed

347    by ATMS and then CTRL and CRIS. However, POD results manifest that ATMS performs best

348   (1 is perfect) and CONV is worst. The different statistics of forecast verification may depend on

349   the purpose of the verification, and the results we evaluated by different methods can explain the

350   different question we want to answer. Overall, the results reflect that DA has a positive effect on

351   reproducing the monthly mean daily precipitation in the TP compared with CTRL to varying

352   degrees.

353

354   *4.2 Impact of DA on the temporal distribution of precipitation forecast*

355       Another measure of performance is to examine how the daily precipitation is temporally

356   distributed (Fig. 8). It can be seen in the time series of Figure 8a that there are four observed

357   heavy rainfall events (3.0 mm/day) during the periods of 3–5, 8-10,13–16 and 22–25 July (Fig.

358   8a). In general, the F24H amount of precipitation is overestimated in all three DA experiments

359   by 20%,40%,and 37% for CONV, ATMS, and CRIS, respectively. In contrast, of the 4 heavy

360   rainfall periods, 3 events including 3–5, 13–16 and 22–25 July are underestimated (grey

361   shadings). The L24H forecasts (Fig. 8b) showed a similar behavior, except that there were much

362   smaller differences among the three DA experiments compared with the F24H forecasts. The

363   F24H forecasts appear the one-day time lag effect compared with L24H. Because the F24H

364   forecasts calculate the cumulative precipitation of the first 6-30 hour while the L24H forecasts

365   represent the 30-54 hour cumulative precipitation forecasts. When all the overestimation events

366   are considered, the CONV (blue line) experiment captured the accumulated amount of

367   precipitation much more accurately than the other DA experiments and the ATMS (red line)

368  performed the worst. It is usual to define the amount of 25.0 to 49.9 mm and superior to 50 mm

369  daily precipitation as heavy rain and thunderstorm, respectively. However, due to the history data

370  sets of the TP indicating that the days of precipitation exceeding 50 mm are few (only accounting

371  for 0.3% of rain days) (Wei et al., 2003) and referring to previous studies (Wang et al., 2011;

372  Zhao et al., 2015), the heavy rainfall threshold was defined as above 20 mm for the 24 h

373  precipitation in this study. As mentioned above, the 24 h precipitation maxima surpassing 20 mm

374  are spread in the main precipitation region, showing that the prominent geographical dependence

375  of rainfall coincides with the threshold of heavy rainfall defined for TP areas.

376      Although previous studies and our results show an obvious trend of overestimating rainfall

377  in the TP, there appears to be underestimated during heavy rainfall events (Fig. 8). To determine

378  the forecast capabilities of the model in the heavy rainfall periods, we focused on the heavy

379  rainfall period of 3-5 July.

380      Figure 9 shows the rainfall intensities (bars) calculated for every 3 h amount of

381  precipitation. The cumulative precipitation (curves) is defined as the precipitation accumulated

382  for each 3 h  starting at 06:00 UTC during 3–6 July. From the perspective of observations, this

383  rainfall event can be divided into three periods, of which the 3 July is ahead of the heavy rainfall

384  with less than 0.45 mm per 3 h, followed by the rainfall around 03:00 UTC on 4 July to 03:00

385  UTC on 5 July, with the first peak at 21:00 UTC on 4 July of more than 0.65 mm per 3 h. The

386  third phase started at 03:00 UTC on 5 July and ended at 00:00 UTC on 6 July with a second

387  rainfall pulse around 21:00 UTC on 5 July exceeding 0.60 mm per 3 h and then weakening. It is

388  evident that this rainfall event had a significant diurnal harmonic and the maximum precipitation

389  always occurred at 18:00–21:00 UTC (00:00–03:00 LST). This diurnal variation was remarkable,

390  especially when the heavy rainfall occurred, which was equivalent to evening local solar time

391  (LST). However, the simulated maximum always occurred at 06:00–09:00 UTC (12:00–15:00

392  LST), earlier than the observations, and can probably be attributed to the limit of complicated

393  topography. In this case, simulated rainfall intensity was much lower than the observations

394  during 09:00 UTC on 4 July to 00:00 UTC on 5 July and 12:00 UTC on 5 July to 21:00 UTC on

395  5 July when the rainfall occurred. That is, the model cannot promptly quantitatively predict the

396  sudden occurrence of this event. Moreover, the cumulative curves of the model show an

397  overestimation on 3 and 5 July compared with observations; in particular, the cumulative curves

398  of the CTRL are far away from the measured values due to an inaccurate initial field. It can be

399  concluded that the DA experiments data are closer to the observations during the heavy rainfall

400  period compared with the CTRL experiment.

401

402  *4.3 Impact of DA on circulation and water vapor supply*

403  According to the above-mentioned analysis, it is evident that DA improves forecasts during

404  the heavy rainfall period, but the results are not the same when different data sets are injected. As

405  is well known, adequate water vapor transport is one of the preconditions for precipitation

406  formation. In this section, we discuss the water vapor supply in the 3–5 July case study, with the

407  aim of determining the reason for the different influences exerted by different experimental

408    schemes. Figure 10 shows the F24H forecasts of precipitation quantity (shadings) and water

409    vapor flux (vectors) during 3–5 July. Zonal component of wind velocity (u), meridional

410    component of wind velocity (v),  specific humidity (q), and covariance, which are needed for

411    flux computations, are provided at eight standard pressure levels (1000, 925, 850, 700, 600, 500,

412    400, and 300 hPa). The equation of water vapor flux for unit length, integrated from the surface

413    to the top of the atmosphere (unit: $kg*m^{-1}*s^{-1}$) and averaged in time atmospheric water vapor

414    flux can be written as:

$$\vec{Q} = Q_u\vec{i} + Q_v\vec{j} \tag{11}$$

416        The zonal and meridional component of vapor flux is described by:

$$Q_u = \frac{1}{g}\int_p^{P_s} qudp \tag{12},$$

418        and  $$Q_v = \frac{1}{g}\int_p^{P_s} qvdp \tag{13}.$$

419        Where $P_s$ is the surface level and p is the top of atmosphere (10 hPa), g is the gravitational

420    constant ($9.8 \ m*s^{-2}$ ).

421        The water vapor flux divergence (D, unit: $kg \bullet m^{-2} \bullet s^{-1}$) is given by:

$$D = \frac{\partial Q_u}{a \cos \varphi \, \partial \sigma} + \frac{\partial Q_v}{a \, \partial \varphi} \tag{14}$$

423        where a is the radius of the model earth taken as 6371.2 km, $\varphi$ is latitude in radians,

424    and $\sigma$ is longitude in radians.

425        According to observations, warm and humid water vapor is transferred from the Bay of

426    Bengal eastward by the southwest monsoon. The TP blocks the westward transport of humid and

427    warm air, and this rainfall event start developing in the southeast of the TP on 3 July and then the

428   rainbelt runs southeast to southwest and develops along the Himalayas on 4–5 July. Comparing

429   the observations (Fig. 10a–c) with model results (Fig. 10d–f), the simulated precipitation is

430   considerably larger than the observed on 3 July before the heavy rainfall occurs, but as time goes

431   on this condition reverses. For the difference value distribution (Fig. 10g–i) of the CTRL minus

432   observations, the main water vapor flux divergence differences (shadings) are negative in the

433   rainy region on 3 July, which indicates that the water vapor convergence is stronger than

434   observed, inducing the overestimation. However, when the rainfall event occurs on 4–5 July, this

435   condition is opposite. The water vapor differences (vectors) also suggest that the observed water

436   vapor conveyance from the southeastern of the TP is larger than the model simulation, which

437   induces inaccuracies in the forecast of the heavy rain. Therefore, analysis of moisture is useful

438   for improving the heavy rainfall forecasting skill.

439      To further discuss the effect of DA on this rainfall event, the differences between the

440   simulated F24H precipitation and the observed distribution and the FSS skill scores (Fig. 11)

441   were considered. From the spatial distribution, all the experiments (Fig. 11a, d, g, j)

442   overestimated the precipitation quantity, especially the CTRL, before the heavy rainfall and the

443   FSS skill scores all ranged from 0.46 to 0.49 with little differences (bottom left in Fig. 11m).

444   When the heavy rainfall event occurred on 4 July, the observed rainbelt moved southwest (Fig.

445   11b, e, h, k), while the simulated rainbelt was motionless, leading to an underestimation in the

446   southwest. The FSS scores for ATMS, CONV and CTRL ranged from 0.42 to 0.48 (middle in

447   Fig. 11m), but CRIS only scored 0.36. As the water vapor conveyance directly contributes to the

448 westward movement of the rainbelt and the intensity of this precipitation event on 5 July, the

449 precipitation experiments all underestimated the amount of precipitation, and CRIS performed

450 particularly badly (Fig. 10c, f, i). However, ATMS had a substantially high FSS scores (0.47)

451 (right in Fig. 11m), followed by CRIS (0.45) and CONV (0.43) while CTRL only scored 0.35.

452 This result indicates that DA can indeed improve the heavy rainfall forecast. From the above

453 analysis of Figure 9 and 11, it is clear that before the heavy rainfall, DA can improve the

454 simulation of precipitation spatially. As time passes and the heavy rainfall develops, DA,

455 especially the ATMS assimilation, can enhance model prediction abilities both spatially and

456 temporally in comparison with the CTRL experiment.

457

458 **5. Summary and discussion**

459    In this study, we used diagnostic methods to analyze the impact of DA on the monthly

460 precipitation distribution over the TP and then focused on one heavy rainfall case study that

461 occurred from 3 to 5 July 2015. The DA and NWP were performed for July 2015 to make the

462 weather forecasts. The spatial distribution of monthly mean precipitation showed an evident rain

463 shadow effect along the Himalayas and that the precipitation decreased northward in the TP.

464 However, the simulated precipitation belt was shifted northward compared with the observed

465 rainbelt and showed an orographic bias described as an overestimation in the upwind of the

466 mountains and an underestimation in the south of the rainbelt. Assimilation of satellite radiance

467 also can not calibrate the rain shadow effect and all experiments showed consistently gross

468    overestimation patterns. Furthermore, it seems that the rain shadow mainly influences prediction

469    of the quantity of precipitation, but the main rainfall pattern can be well predicted. The pattern,

470    which false alarms are primarily predicted in the east of the TP and the misses in the west,

471    indicates that the WRF-ARW model has promising potential to improve weather forecast ability.

472    The DA validation statistics also suggest that DA has a positive effect on monthly mean

473    precipitation prediction in the TP compared with the CTRL to varying degrees. For the time

474    series of monthly precipitation, F24H and L24H precipitation chiefly overestimate the amount of

475    precipitation, which is in agreement with previous studies, but the amount of 24 h precipitation

476    in the three heavy rainfall periods of 3–5, 13–16, and 22–25 July is underestimated.

477    To further study the underestimations in the heavy rainfall events and the performance of the

478    WRF-ARW model and GSI DA impact, we selected a case study from 3 to 5 July. It is evident

479    that this rainfall event had a significant diurnal harmonic and the maximum precipitation always

480    occurred at 18:00–21:00 UTC (00:00–03:00 LST). This diurnal variation was remarkable,

481    especially when the heavy rainfall occurred. Although the model can not promptly quantitatively

482    predict the sudden occurrence of this rainfall event, the DA, especially the ATMS simulation are

483    closer to the observations for the heavy rainfall event compared to CTRL experiments. Overall,

484    before the heavy rainfall, DA improved the precipitation prediction spatially. As time passed and

485    the rainbelt moved and rainfall developed, DA enhanced the model prediction abilities both

486    spatially and temporally. It should be mentioned that the high altitude and complex topography

487    of the TP and its blocking effect on moisture transfer coming from Indian Ocean by the

488    southwest monsoon obviously influences the rainfall forecast. As precipitation biases indicate

489    some extent of spatial coherence and temporal recurrence, it is possible to provide an adapted

490    correction method to enhance the model precipitation prediction capabilities.

491        It is conspicuous that the ATMS showed better performance than CTRL, CONV, and CRIS

492    in the case study. Past studies have indicated that the effect of assimilation of both observations

493    and satellite products is better than assimilation of satellite data only, which may account for the

494    ATMS performing better than CONV. ATMS also performed better than CRIS. As clouds are

495    opaque in the infrared wave band of the spectrum and largely transparent in the microwave band,

496    microwave instruments are thought to perform better than infrared instruments on cloudy and

497    rainy days, which may explain the better performance of ATMS compared with CRIS.

498        In this study, we investigated the monthly precipitation distribution and a selected heavy

499    rainfall case in the TP using the WRF-ARW mesoscale model and the GSI data assimilation

500    system. Moisture and dynamic conditions were analyzed in the case study; however, thermal

501    conditions are also one of the direct factors leading to rainfall that need to be investigated in the

502    future.

503        Furthermore, although the CrIS were assimilated large amount of satellite radiance pixels,

504    the general DA effect is relatively worse compared with the other three experiments. CrIS has

505    1305 spectral channels, some of which are redundant as they include many satellite radiance

506    observations from similar altitudes and contain much repeated information, which may lead to

507    the poor DA impact. It should take the priority to select physical sensitivity and the high vertical

508  resolution channels. Moreover, selecting channels is more difficult because of the high altitude,

509  complicated dynamics and thermal conditions. Therefore, only by carrying out further research

510  on bias correction, quality control, and channel selection can satellite radiance data play an

511  efficient role in TP weather forecasting.

512     In addition, model resolution and parameterized scheme selection are also key factors

513  affecting forecast quality. In this study, the parameterized schemes we choose have been applied

514  in previous studies of the TP. It would be worthwhile to make a comparative analysis of different

515  parameterized schemes with higher model resolution in the future. Furthermore, it should be

516  noted that due to the heavy calculation burden, this study made use of 3D-Var as the assimilation

517  method. Other advanced assimilation techniques, such as 4D-Var, Hybrid, and EnKF, also need

518  to be tested.

519

520  *Acknowledgements*

521  The WRF-ARW model was obtained from NCAR, the GSI data assimilation system was

522  obtained from JCSDA, and the satellite datasets were provided by NOAA/NESDIS/STAR.  The

523  authors are very grateful to these agencies for the model and providing data. This work was

524  jointly supported by the Special Fund for Public Welfare of China Meteorological Administration

525  (GYHY201406024) and the National Natural Science Foundation of China (91437104,

526  41130960). The corresponding author was supported by the National Innovation Project for

527  Meteorological Science and Technology: Quality Control, Fusion, and Reanalysis of

528    Meteorological Observations and the Guangdong Ocean University Research Funding of Air–

529    Sea Interaction and Data Assimilation (300702/E16188). The first author was a visiting scholar

530    at GMU/AOES during this study and acknowledges helpful discussions with fellow members of

531    GMU/AOES.

532

533

**Reference**

Bormann, N., A. Fouilloux, and W. Bell: Evaluation and assimilation of ATMS data in the ECMWF system, *Journal of Geophysical Research: Atmospheres*, *118*(23), 2013

Chambon, P., S. Q. Zhang, A. Y. Hou, M. Zupanski, and S. Cheung: Assessing the impact of pre-GPM microwave precipitation observations in the Goddard WRF ensemble data assimilation system, *Quarterly Journal of the Royal Meteorological Society*, *140*(681), 1219-1235, 2014

Chen, Y., L. Ji, and R. Shen: The numerical experiments on dynamic forcing by the Tibetan Plateau for various zonal flows, *Advances in Atmospheric Sciences*, *2*(2), 189-199, 1985

Derber, J. C., and W. S. Wu: The use of TOVS cloud-cleared radiances in the NCEP SSI analysis system, *Monthly Weather Review*, *126*(8), 2287-2299, 1998

Dong, P., Liu, J., Liu, G., & Huang, J.: Study on the assimilation of ATMS satellite data and comparison with AMSUA/MHS, *Journal of Tropical Meteorology*, 30(4), 623-632, 2014

Eyre, J. R.: A bias correction scheme for simulated TOVS brightness temperatures, *ECMWF Tech. Memo.*, 186, 28, 1992 [Available from European Centre for Medium-Range Weather Forecasts, Shin-field Park, Reading, Berkshire R62 9AX, United Kingdom.]

Gao, Y. C., and Liu, M. F. Evaluation of high-resolution satellite precipitation products using rain gauge observations over the tibetan plateau. *Hydrology & Earth System Sciences Discussions*, 2013, 9(8), 9503-9532.

Gao, Y., J. Xu, and D. Chen: Evaluation of WRF Mesoscale Climate Simulations over the

554   Tibetan Plateau during 1979–2011, Journal of Climate, 28(7), 2823-2841, 2015

555   Gauthier, P., M. Tanguay, S. Laroche, S. Pellerin, and J. Morneau: Extension of 3DVAR to

556       4DVAR: Implementation of 4DVAR at the Meteorological Service of Canada, Mon. Wea.

557       Rev., 135, 2339–2354, 2007

558   Guo, J., Zhai, P., Wu, L., Cribb, M., Li, Z., Ma, Z., & Zhang, J.: Diurnal variation and the

559       influential factors of precipitation from surface and satellite measurements in

560       Tibet, *International Journal of Climatology*, *34*(9), 2940-2956, 2014

561   Han, Y., P. Delst, Q. Liu, F. Weng, B. Yan, R. Treadon, and J. Derber: JCSDA Community

562       Radiative Transfer Model-Version 1 (CRTM-V1), *NOAA Tec,* (122), 40, 2006

563   He, Y., K. Yang, T. Yao, and J. He: Numerical Simulation of a Heavy Precipitation in Qinghai-

564       Xizang Plateau Based on WRF Model, *Plateau Meteorology (in Chinese)*, 31(5), 1185-1186,

565       2012

566   Developmental Testbed Center, 2016 : Gridpoint Statistical Interpolation Advanced User's Guide

567       Version 3.5. Available at http://www.dtcenter.org/com-GSI/users.v3.5/docs/index.php, 119

568       pp.

569   Hubbard, K. G., and J. You: Sensitivity analysis of quality assurance using the spatial regression

570       approach-A case study of the maximum/minimum air temperature, *Journal of Atmospheric*

571       *and Oceanic Technology*, *22*(10), 1520-1530, 2005

572   Kazumori, M.: Satellite radiance assimilation in the JMA operational mesoscale 4DVAR

573       system, *Monthly Weather Review*, *142*(3), 1361-1381, 2014.

574   Liu, J., M. Bray, and D. Han: A study on WRF radar data assimilation for hydrological rainfall

575    prediction, *Hydrology and Earth System Sciences*, *17*(8), 3095-3110, 2013

576    Marteau, R., Y. Richard, B. Pohl, C. C. Smith, and T. Castel: High-resolution rainfall variability

577        simulated by the WRF RCM: application to eastern France, *Climate Dynamics*, *44*(3-4),

578        1093-1107, 2015

579    Massacand, A. C., H. Wernli, and H. C. Davies: Heavy precipitation on the Alpine southside: An

580        upper-level precursor, *Geophysical Research Letters*, *25*(9), 1435-1438, 1998

581    Maussion, F., D. Scherer, R. Finkelnburg, and J. Richters: WRF simulation of a Precipitation

582        event over the Tibetan Plateau, China- An assessment using remote sensing and ground

583        observations, *Hydrol. Earth Syst. Sci.*, 15, 1795-1817, 2011

584    Newman, K. M., C. S. Schwartz, Z. Liu, H. Shao, and X.-Y. Huang: Evaluating Forecast Impact

585        of Assimilating Microwave Humidity Sounder (MHS) Radiances with a Regional Ensemble

586        Kalman Filter Data Assimilation System, *Weather and Forecasting*, *30*(4), 964-983, 2015

587    Pan, Y., Y. Shen, Q.-Q. Yu, and P. Zhao: Merged analyses of gauge-satellite hourly precipitation

588        over China based on OI technique (in Chinese with English abstract), Acta Meteor. Sin, 70,

589        1381-1389, 2012

590    Purser, R. J., Wu, W. S., Parrish, D. F., and Roberts, N. M: Numerical aspects of the application

591        of recursive filters to variational statistical analysis. Part I: Spatially homogeneous and

592        isotropic Gaussian covariances. *Monthly Weather Review*, 131(8), 1524-1535, 2003a

593    Purser, R. J., Wu, W. S., Parrish, D. F., and Roberts, N. M: Numerical aspects of the application

594        of recursive filters to variational statistical analysis. Part II: Spatially inhomogeneous and

595    anisotropic general covariances. *Monthly Weather Review*, 131(8), 1536-1548, 2003b

596    Roberts, N. M., and H. W. Lean: Scale-selective verification of rainfall accumulations from high-

597      resolution forecasts of convective events, Mon. Wea. Rev., 136, 78–97, 2008

598    Saunders, R., M. Matricardi, and P. Brunel: An improved fast radiative transfer model for

599      assimilation of satellite radiance observations, *Quarterly Journal of the Royal*

600      *Meteorological Society*, *125*(556), 1407-1425, 1999

601    Schwartz, C. S., Z. Liu, Y. Chen, X. Y. Huang: Impact of assimilating microwave radiances with

602      a limited-area ensemble data assimilation system on forecasts of Typhoon Morakot, *Weather*

603      *and Forecasting*, *27*(2), 424-437, 2012.

604    Shen, Y., P. Zhao, Y. Pan, and J. Yu: A high spatiotemporal gauge-satellite merged precipitation

605      analysis over China, *Journal of Geophysical Research: Atmospheres*, *119*(6), 3063-3075,

606      2014.

607    Tong, K., Su, F., Yang, D., and Hao, Z. Evaluation of satellite precipitation retrievals and their

608      potential utilities in hydrologic modeling over the tibetan plateau. *Journal of Hydrology*,

609      2014, 519, 423–437.

610    Wang, C. H., S. W. Zhou, X. P. Tang, and P. Wu: Temporal and spatial distribution of heavy

611      precipitation over Tibetan Plateau in recent 48 years, *Scientia Geographica Sinica*, *31*(4),

612      470-477, 2011.

613    Warner T. T., R. A. Paterson, and R. E. Treadon, 1997: A tutorial on lateral boundary conditions

614      as a basic and potentially serious limitation to regional numerical weather prediction. Bull.

615 Amer. Meteor. Soc., 78, 2599-2617.

616 Wei, Z., R. H. Huang, W. J. Dong: Interannual and interdecadal variations of air temperature and

617 precipitation over the Tibetan Plateau, *Chinese Journal of Atmospheric Sciences*, 27(2), 157-

618 170, 2003

619 Weng, F.: Advances in radiative transfer modeling in support of satellite data assimilation.

620 *Hyperspectral Imaging and Sensing of the Environment* (p. HWD1), Optical Society of

621 America, 2009

622 Wu, W., R. Purser, and D. Parrish: Three-Dimensional Variational Analysis with Spatially

623 Inhomogeneous Covariances. *Mon. Wea. Rev.*, 130, 2905–2916, 2002

624 Xie, P., and A. Y. Xiong: A conceptual model for constructing high-resolution gauge-satellite

625 merged precipitation analyses, *Journal of Geophysical Research: Atmospheres*, 116(D21) ,

626 2011

627 Xu, J., S. Rugg, L. Byerle, and Z. Liu: Weather forecasts by the WRF-ARW model with the GSI

628 data assimilation system in the complex terrain areas of southwest Asia, *Weather and*

629 *Forecasting*, *24*(4), 987-1008, 2009

630 Xu, J., B. Zhang, M. Wang, and H. Wang: Diurnal variation of summer precipitation over the

631 Tibetan Plateau: a cloud-resolving simulation, *Annales Geophysicae,* 30(11), 1575-1586,

632 2012

Xu, J. and A. Powell: Dynamical downscaling precipitation over the Southwest Asian: impacts of radiance data assimilation on the hindcasts of the WRF-ARW model, Atmos. Res., 111, 90–103, 2012

Ye, D. Z., and Y. X. Gao: Tibetan Plateau Meteorology. *Science, Beijing*, 89-101, 1979

Zapotocny, T. H., J. A. Jung, J. F. Le Marshall, and R. E. Treadon: A two-season impact study of four satellite data types and rawinsonde data in the NCEP Global Data Assimilation System, *Weather and Forecasting*, *23*(1), 80-100, 2008

Zhang, X., X, B., & X, K.: Observed diurnal cycle of summer precipitation over South Asia and East Asia based on CMORPH and TRMM satellite data, *Atmospheric and Oceanic Science Letters*, *8*(4), 201-207, 2015

Zhao, X. Y., Y. R. Wang, Q. Zhang, and L. Luo: Climatic characteristics of heavy precipitation events during summer half year over the Eastern Tibetan Plateau in recent 50 years, *Arid Land Geography*, *4*, 004, 2015.

Zhu, F., G. Xu, and L. Li: An assessment of the impact on precipitation prediction in the middle and lower reaches of the Yangtze River made by assimilating GPSPW data in the Tibetan Plateau, *Chinese Journal of Atmospheric Sciences (in Chinese)*, 38 (1): 171–189, 2014

Zou, X., Z. Qin, and F. Weng: Improved coastal precipitation forecasts with direct assimilation of GOES-11/12 imager radiances, *Monthly Weather Review*, *139*(12), 3711-3729, 2011

Zou, X., Z. Qin, and F. Weng: Improved quantitative precipitation forecasts by MHS radiance data assimilation with a newly added cloud detection algorithm, *Monthly Weather Review*, *141*(9), 3203-3221, 2013.

654

**Table 1.** The channels for ATMS and CrIS data that have been selected for the data assimilation procedure

| Sensor | Channels |
|--------|----------|
| ATMS | 1-14, 16-22 |
| CrIS | 37, 49, 51, 53, 59, 61, 63, 65, 67, 69, 71, 73, 75, 77, 79, 80, 81, 83, 85, 87, 89, 93, 95, 96, 99, 101, 102, 104, 106, 107, 116, 120,123, 124,,125, 126, 130, 132, 133, 136, 137, 138, 142,143, 144, 145, 147, 148, 150, 151, 153, 154, 155, 157-168, 170, 171, 173, 175, 198, 211, 224, 279, 342, 392, 404, 427, 464, 482, 501, 529 |

**Table 2.** Rain contingency table used in the verification studies. As a threshold, 6 mm day$^{-1}$ is chosen to separate rain from no-rain events

| Forecast | Observed | |
|----------|----------|----|
| | Yes | No |
| Yes | Hits | False alarms |
| No | Misses | Correct rejections |

     **Figure captions**

668     **Figure 1.** (a) Simulation domains and topography. Resolutions are at 12 km and 4 km for the

669              outer (coarse grid, D01) and inner (nested grid, D02) boxes, respectively. The shading

670              indicates the terrain elevation (unit: m). (b)–(d) Distribution of (b) conventional data

671              observations, (c) scan coverage of ATMS data after data assimilation, and (d) scan

672              coverage of CrIS data after data assimilation at 06:00 UTC on 1 July 2015.

673     **Figure 2.** Blue bars indicate the total amount of radiance read in the DA system. Red bars

674              present the number of kept radiance after first step of quality control. The used

675              percentage after final quality control is shown as black curves. The right y-axis

676              indicates the ratio of used amount to read amount and the ratio is expressed as percent.

677              Top panel is for ATMS (a) and bottom is for CrIS data (b).

678     **Figure 3.** Top panel shows the schematic of data assimilation configuration with 3D-Var. Bottom

679              panel presents the experiments design. CTRL: control experiment without data

680              assimilation that the initial time is 00:00 UTC from 1 to 31 July; CONV: data

681              assimilation with conventional data only; ATMS: data assimilation with conventional

682              and ATMS data; CRIS: data assimilation with conventional and CrIS data. CONV,

683              ATMS and CRIS experiments all start at 06:00 UTC from 1 to 31 July.

684     **Figure 4.** Daily precipitation averaged (unit: mm) for the month of July 2015. (a), (b) are F24H

685              forecast and (c), (d) are L24H forecast. Black contours are altitude (unit: m).

686     **Figure 5.** Difference value distribution of monthly mean precipitation (unit: mm) during July for

687   data assimilation minus observation experiments. (a), (e) CTRL minus OBS; (b), (f)

688   CONV minus OBS; (c), (g) ATMS minus OBS (d),(h) CRIS minus OBS for (a)–(d)

689   F24Hforecast and (e)–(h) L24Hforecast. Black contours are altitude (unit: m).

690 **Figure 6.** Spatial patterns of (a)–(d) the contingency table and (e)–(h) the scatter plots (monthly

691   mean F24 h rainfall over 6 mm/day threshold is defined as an "event"). The solid grey

692   line indicate the regression line of A. Black contours are altitude (unit: m).

693 **Figure 7.** Monthly and domain average validation statistics for F24H forecast (a–f) and L24H

694   forecast (g–l). (a) and (g) are Bias Score; (b) and (h) are Fraction skill Score; (c) and (i)

695   are Equitable Threat Score; (d) and (j) are Probability of Detection; (e) and (k) are

696   Probability of False Detection; (f) and (l) are False Alarm ratio.

697 **Figure 8.** Time series of daily precipitation distribution for F24H forecast (a) and L24H forecast

698   (b). The black, grey, blue, red and green lines indicate observation, CTRL, CONV,

699   ATMS and CRIS, respectively. The unit is mm. The grey shadings indicate the

700   underestimated events.

701 **Figure 9.** Rainfall intensities (bars) calculated for every 3 h amount of precipitation. The

702   cumulative precipitation (curves) is defined as the precipitation accumulated for each 3

703   h starting at 06:00 UTC during 3–5 July. The unit is mm.

704 **Figure 10.** (a)–(f) 24 h forecasts of precipitation quantity (shadings) and water vapor flux

705   (vectors) during 3–5 July for (a)–(c) OBS and (d)–(f) CTRL. (g)–(i) Differences in

706   water vapor flux (vectors) and water vapor divergence (shadings) between CTRL and

707        OBS. The unit of precipitation is mm. The units for water vapor flux and divergence is

708        kg/(m*s) and kg/(m$^2$*s), respectively.

709    **Figure 11.** (a)–(l) are differences between the simulated F24H precipitation and the observed

710        distribution and (m) is the FSS skill scores with 8 mm/day threshold during 3–5 July.

711        The unit of differences is mm.

712
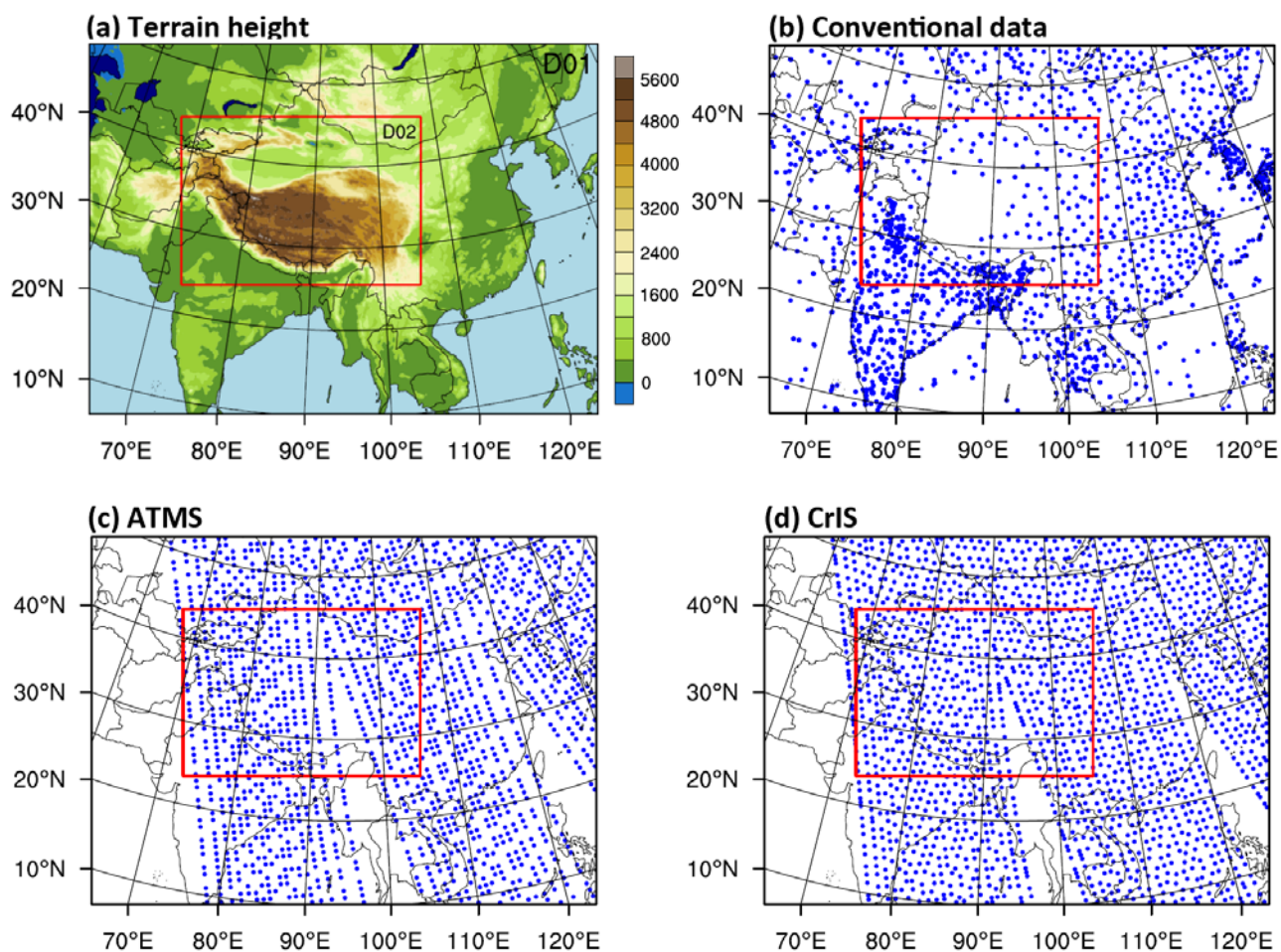
**Figure 1.** (a) Simulation domains and topography. Resolutions are at 12 km and 4 km for the outer

(coarse grid, D01) and inner (nested grid, D02) boxes, respectively. The shading indicates the terrain

elevation (unit: m). (b)–(d) Distribution of (b) conventional data observations, (c) scan coverage of

ATMS data after data assimilation, and (d) scan coverage of CrIS data after dta assimilation at 06:00

UTC on 1 July 2015.

718
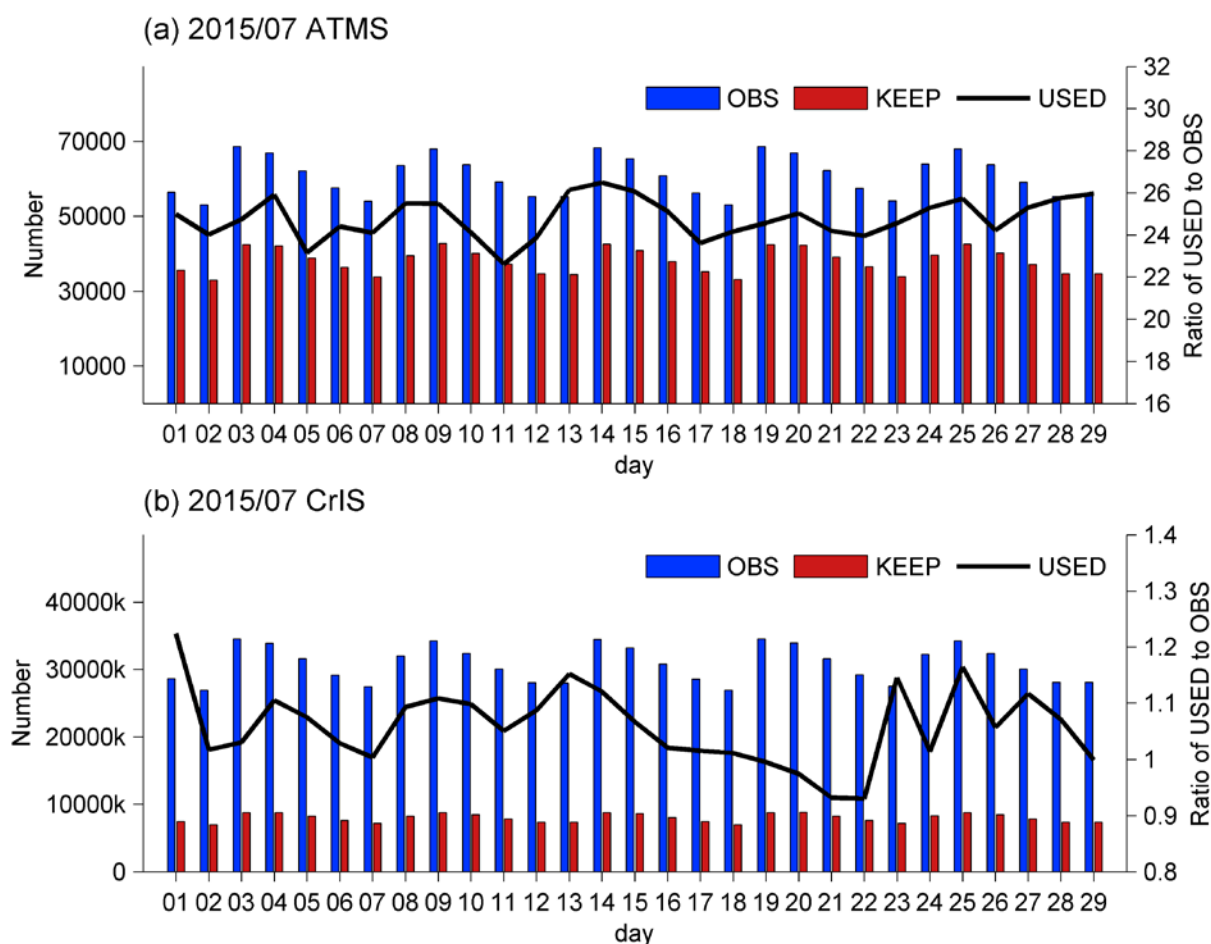
**Figure 2.** Blue bars indicate the total amount of radiance read in the DA system. Red bars present the

number of kept radiance after first step of quality control. The used percentage after final quality

control is shown as black curves. The right y-axis indicates the ratio of used amount to read amount

and the ratio is expressed as percent. Top panel is for ATMS (a) and bottom is for CrIS data (b).
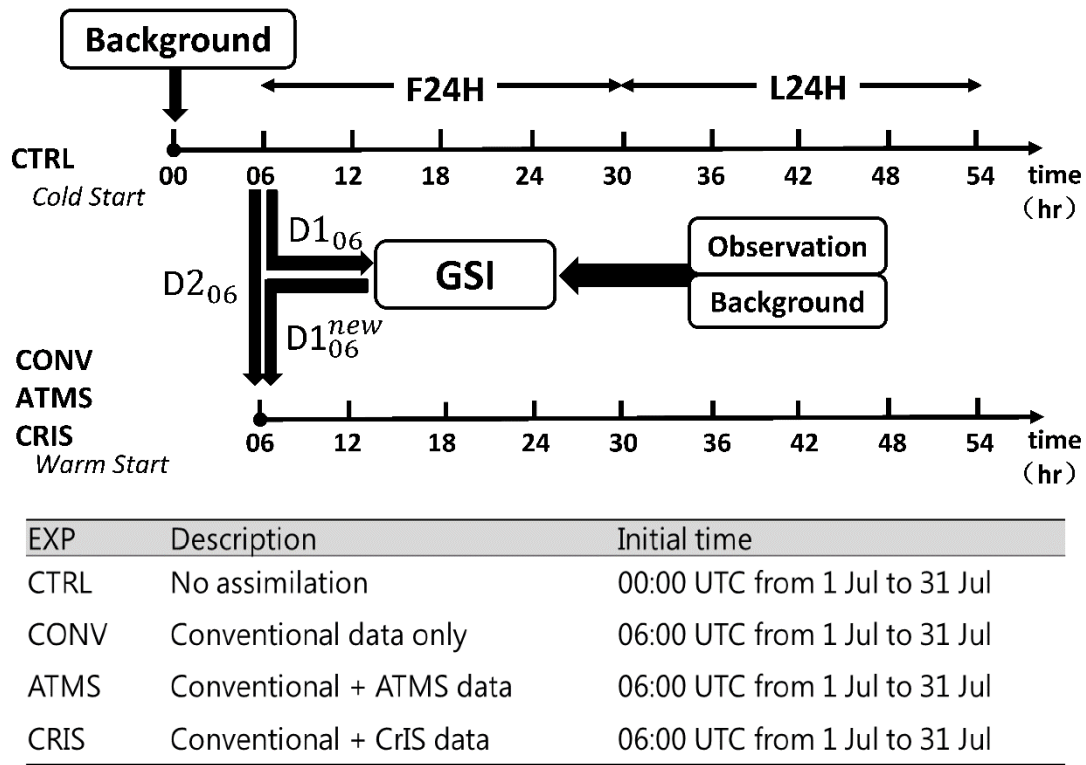
723

| EXP | Description | Initial time |
|---|---|---|
| CTRL | No assimilation | 00:00 UTC from 1 Jul to 31 Jul |
| CONV | Conventional data only | 06:00 UTC from 1 Jul to 31 Jul |
| ATMS | Conventional + ATMS data | 06:00 UTC from 1 Jul to 31 Jul |
| CRIS | Conventional + CrIS data | 06:00 UTC from 1 Jul to 31 Jul |

724

725 **Figure 3.** Top panel shows the schematic of data assimilation configuration with 3D-Var. Bottom

726 panel presents the experiments design. CTRL: control experiment without data

727 assimilation that the initial time is 00:00 UTC from 1 to 31 July; CONV: data assimilation

728 with conventional data only; ATMS: data assimilation with conventional and ATMS data;

729 CRIS: data assimilation with conventional and CrIS data. CONV, ATMS and CRIS

730 experiments all start at 06:00 UTC from 1 to 31 July.

731
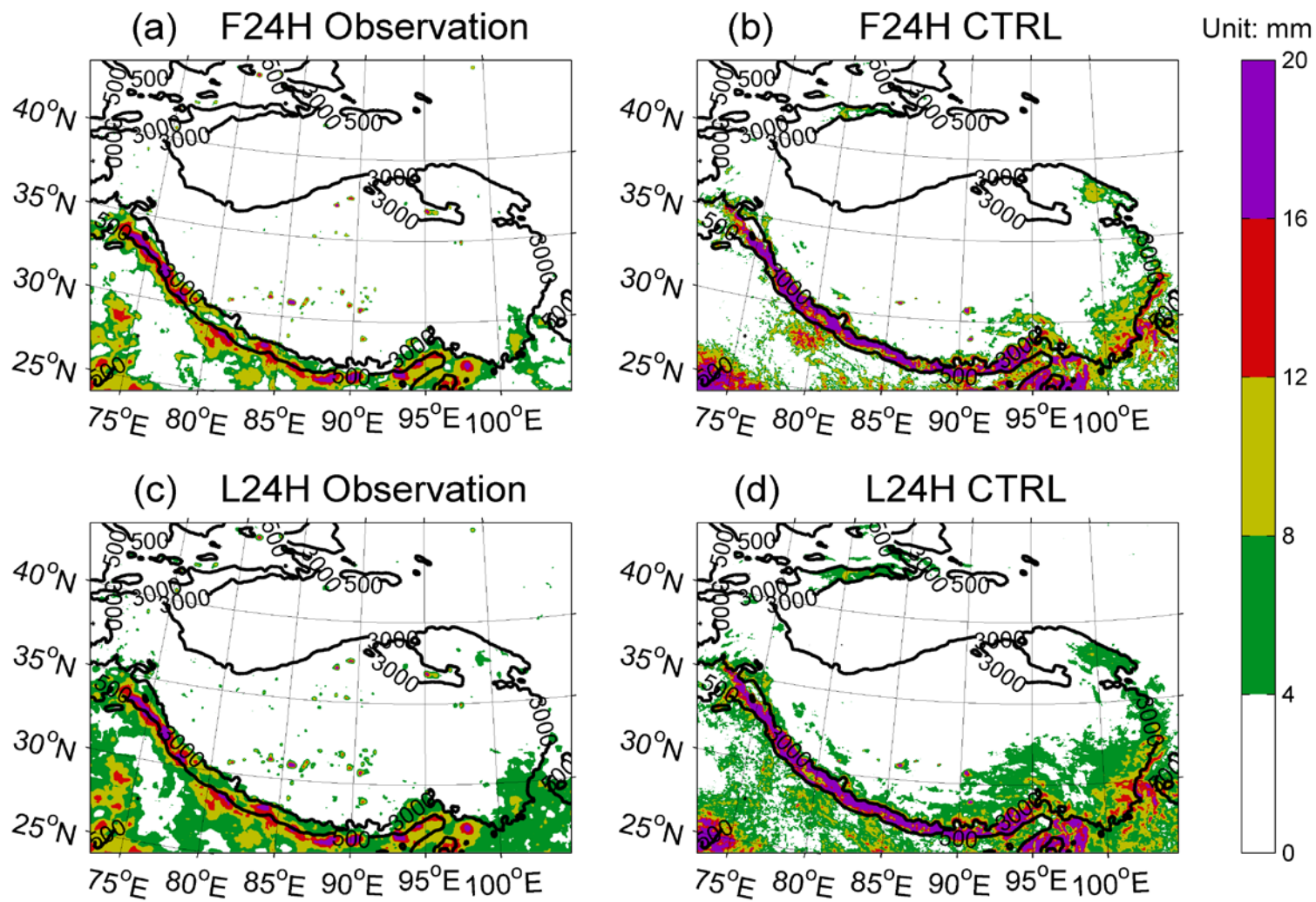
**Figure 4.** Daily precipitation averaged (unit: mm) for the month of July 2015. (a), (b) are F24H forecast and (c), (d) are L24H forecast. Black contours
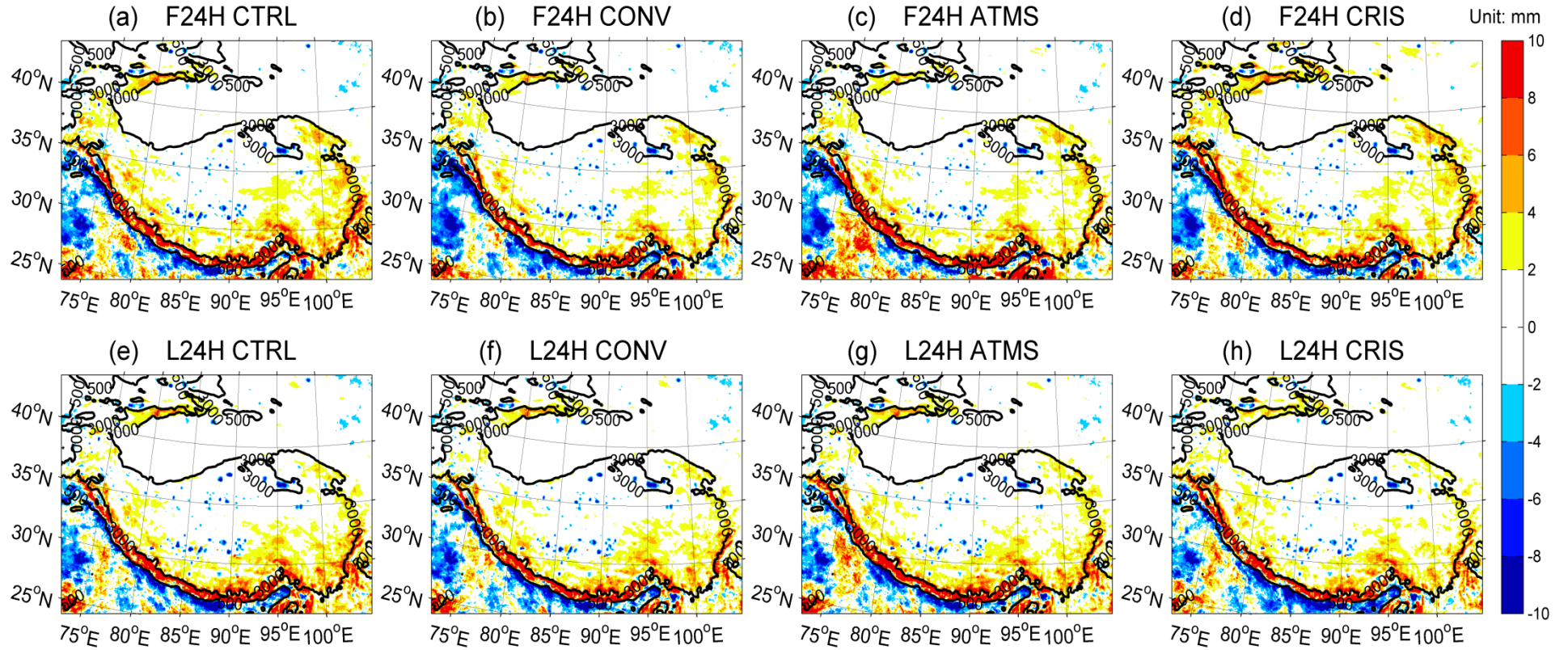
are altitude (unit: m).

**Figure 5.** Difference value distribution of monthly mean precipitation (unit: mm) during July for data assimilation minus observation experiments. (a), (e) CTRL minus OBS; (b), (f) CONV minus OBS; (c), (g) ATMS minus OBS (d),(h) CRIS minus OBS for (a)–(d) F24Hforecast and (e)–(h) L24Hforecast. Black contours are altitude (unit: m).

734

735
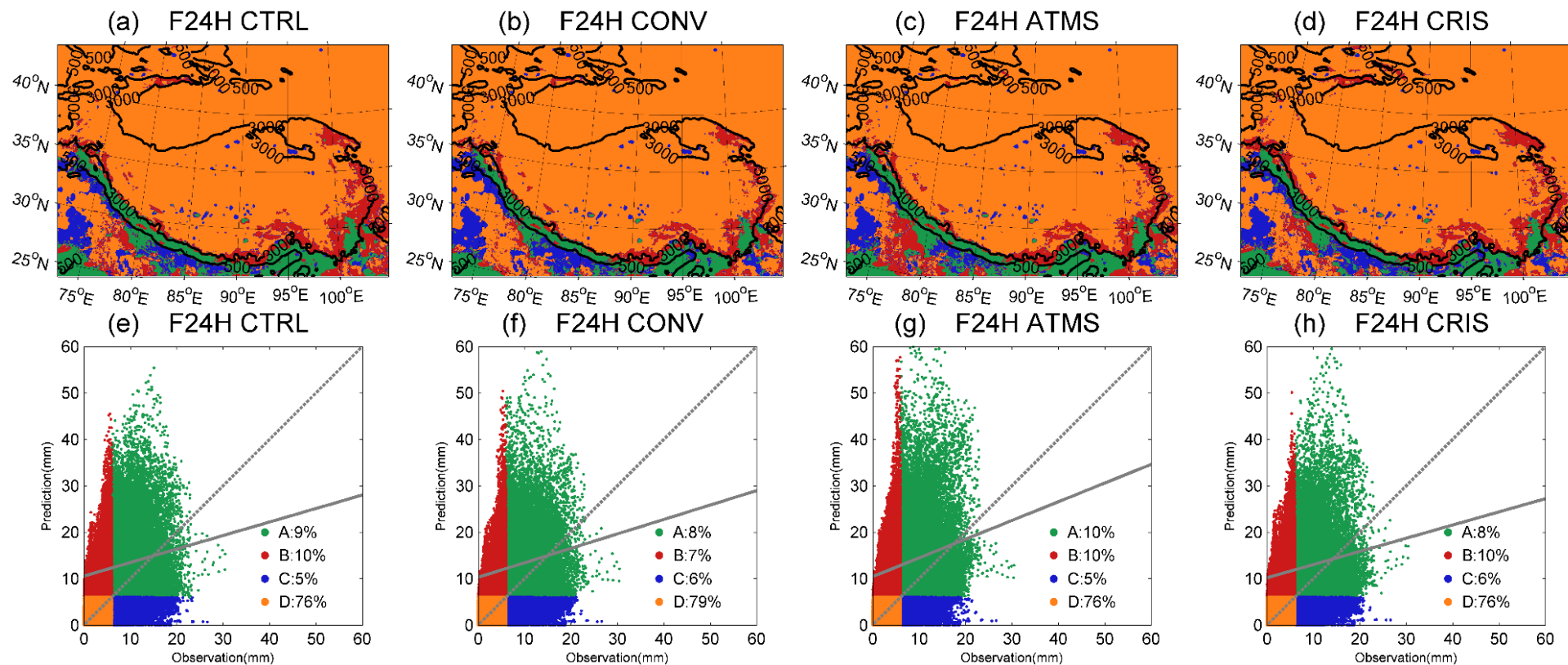
**Figure 6.** Spatial patterns of (a)–(d) the contingency table and (e)–(h) the scatter plots (monthly mean 24 h rainfall over 6 mm/day threshold is defined

as an "event"). A, B, C and D indicate the Hits, False alarms, Misses and Correct rejections in Table 2, respectively. The solid grey lines indicate the

regression line of A. Black contours are altitude (unit: m).
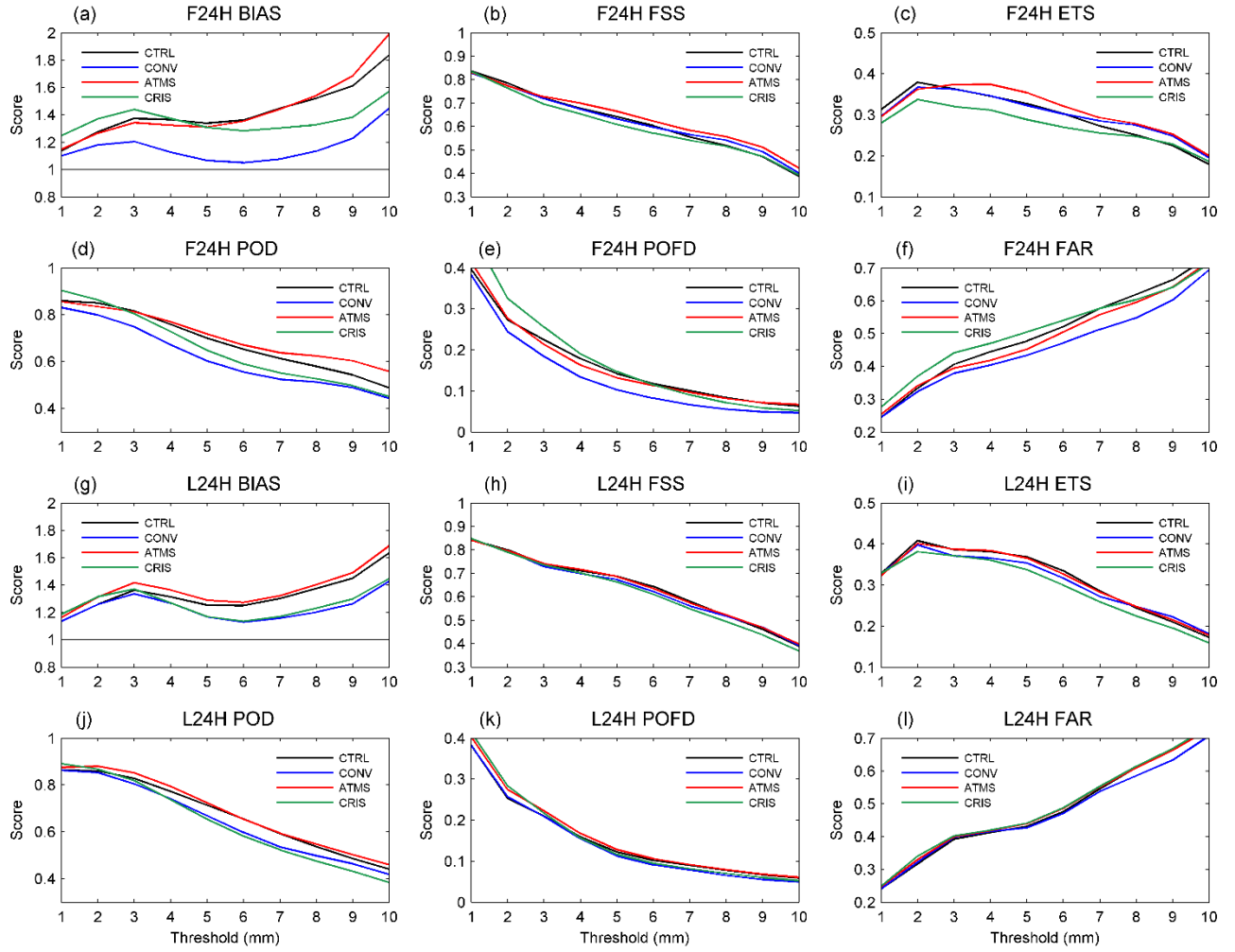
739

**Figure 7.** Monthly and domain average validation statistics for F24H forecast (a–f) and L24H

forecast (g–l). (a) and (g) are Bias Score; (b) and (h) are Fraction skill Score; (c) and (i) are Equitable

Threat Score; (d) and (j) are Probability of Detection; (e) and (k) are Probability of False Detection;
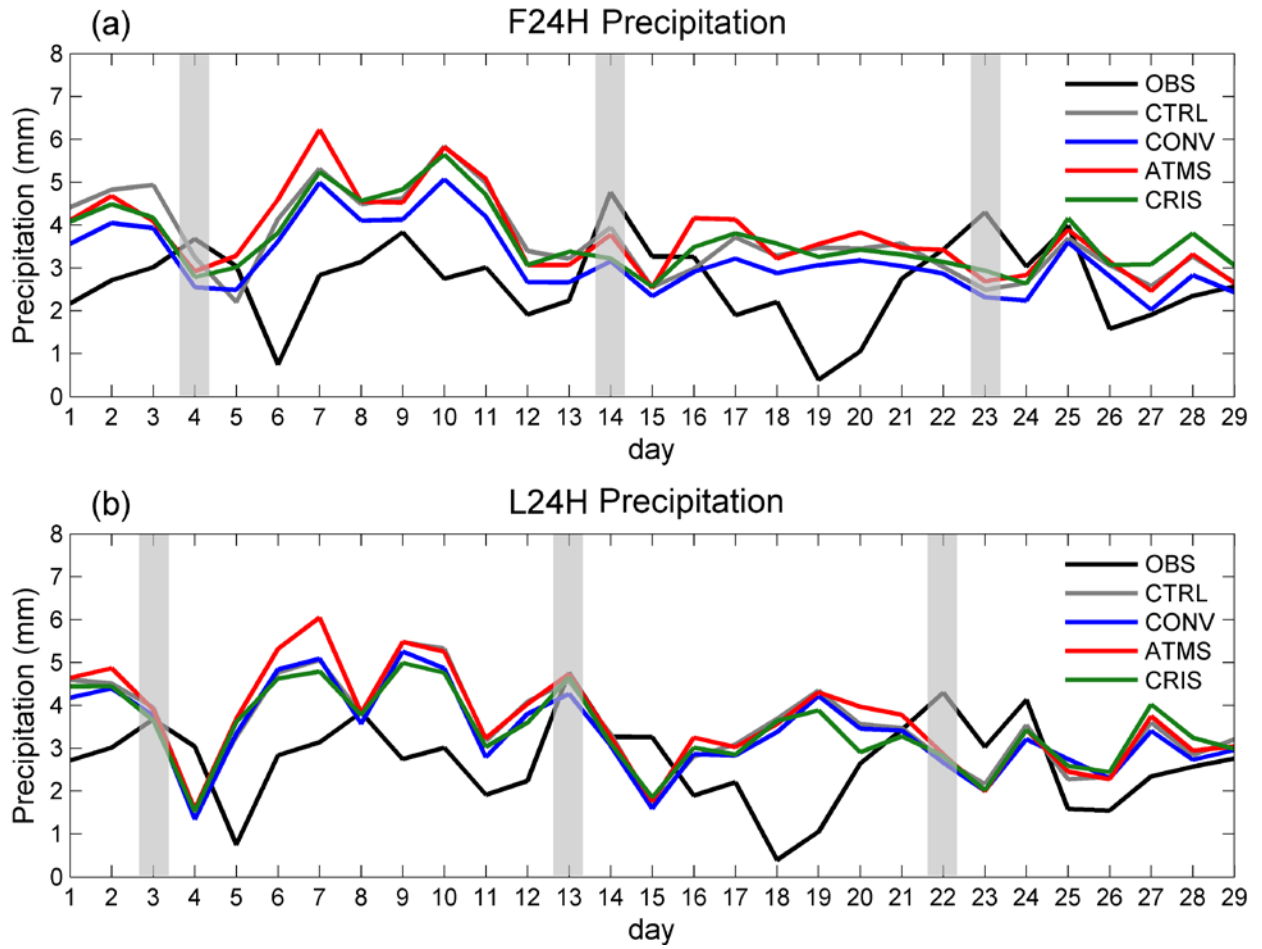
(f) and (l) are False Alarm ratio.

744

**Figure 8.** Time series of daily precipitation distribution for F24H forecast (a) and L24H forecast (b).

746   The black, grey, blue, red and green lines indicate observation, CTRL, CONV, ATMS and CRIS,

747   respectively. The unit is mm. The grey shadings indicate the underestimated events.
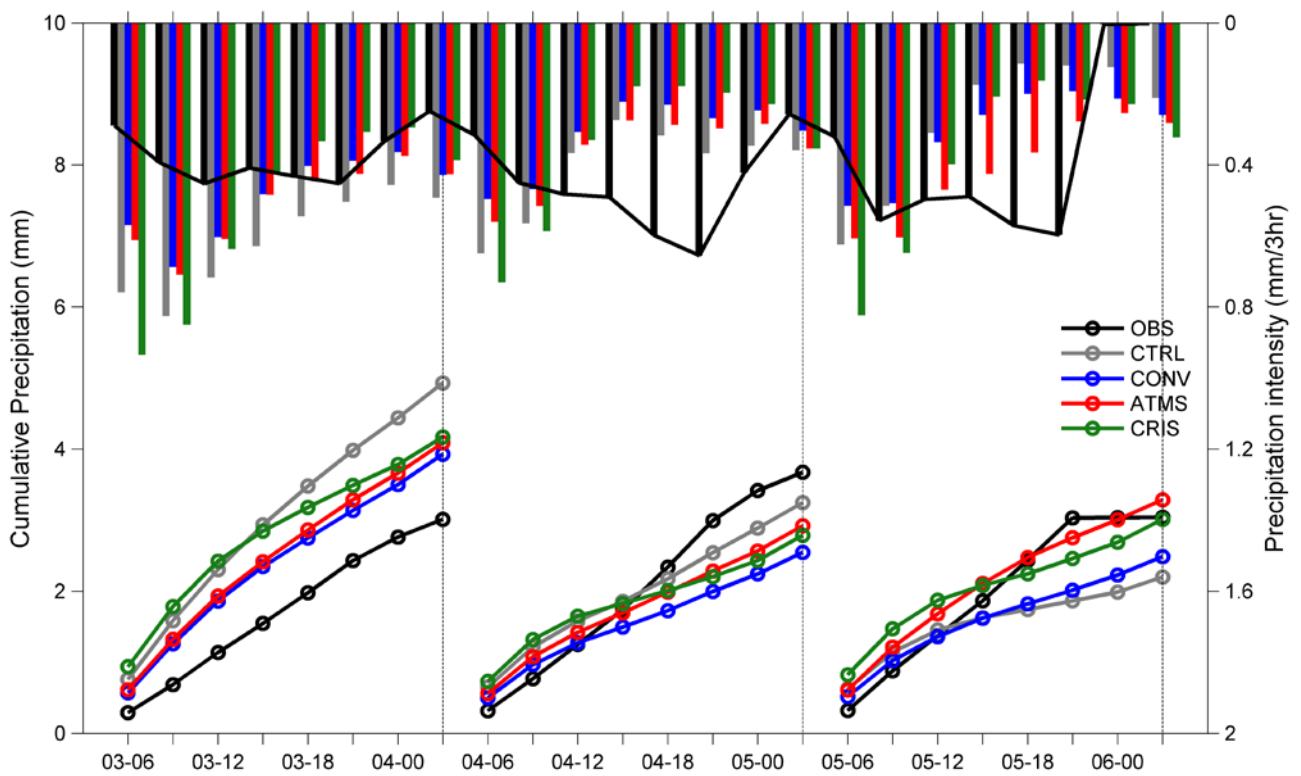
748

749

**Figure 9.** Rainfall intensities (bars) calculated for every 3 h amount of precipitation. The cumulative

precipitation (curves) is defined as the precipitation accumulated for each 3 h starting at 06:00 UTC

during 3–5 July. The unit is mm.

753
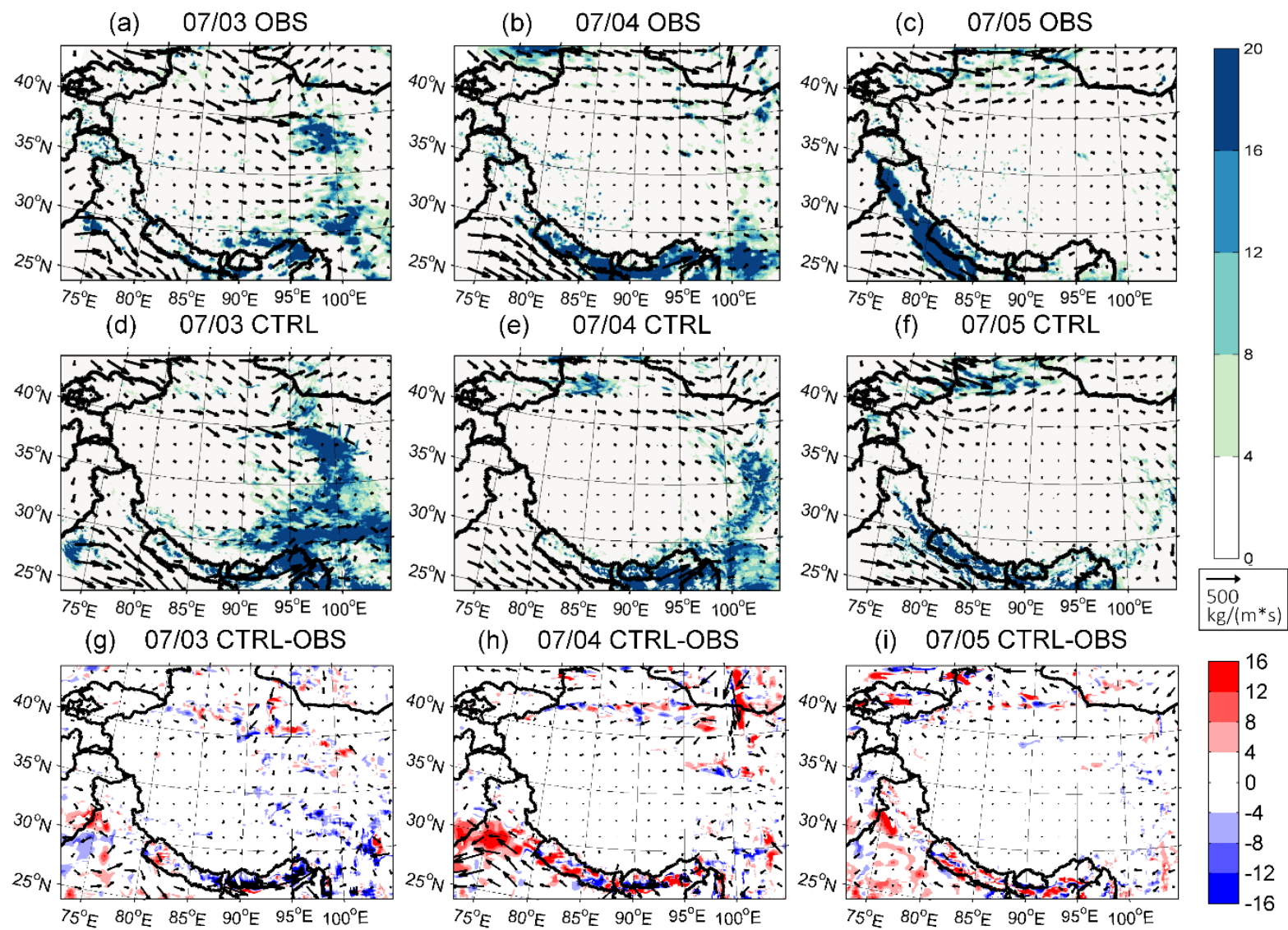
754    Figure 10. (a)–(f) F24H forecasts of precipitation (shadings) and water vapor flux (vectors) during 3–5 July for (a)–(c) OBS and (d)–(f) CTRL. (g)–(i)

755    Differences in water vapor flux (vectors) and water vapor divergence (shadings) between CTRL and OBS. The unit of precipitation is mm. The units for

756    water vapor flux and divergence is kg/(m*s) and kg/(m$^2$*s), respectively.

**Figure 11.** (a)–(l) are differences between the simulated F24H precipitation and the observed distribution and (m) is the FSS skill scores with 8 mm/day threshold during 3–5 July. The unit of differences is mm.